Nanoscale

Selectivity of Nitrate and Chloride Ions in Microporous Carbons: The Role of Anisotropic Hydration and Applied Potentials

Journal:	*Nanoscale*
Manuscript ID	NR-ART-06-2020-004496.R1
Article Type:	Paper
Date Submitted by the Author:	07-Sep-2020
Complete List of Authors:	Aydin, Fikret ; Lawrence Livermore National Laboratory, Material Science Division Ceron, Maira; Lawrence Livermore National Laboratory, Physical and Life Sciences Hawks, Steven; Lawrence Livermore National Laboratory, PLS MSD Oyarzun, Diego; Lawrence Livermore National Laboratory, PLS MSD Zhan, Cheng; Lawrence Livermore National Laboratory, Material Science Division Pham, Tuan; Lawrence Livermore National Laboratory, Condensed Matter and Materials Division Stadermann, Michael; Lawrence Livermore National Laboratory, Campbell, Patrick; Lawrence Livermore National Laboratory, Physical and Life Sciences Directorate

Selectivity of Nitrate and Chloride Ions in Microporous Carbons: The Role of Anisotropic Hydration and Applied Potentials

Fikret Aydin, Maira R. Cerón, Steven A. Hawks, Diego I. Oyarzun, Cheng Zhan, Tuan Anh Pham,* Michael Stadermann,* and Patrick G. Campbell*

Physical and Life Sciences Directorate, Lawrence Livermore National Laboratory, Livermore, CA 94550, USA

Abstract

Understanding ion transport in porous carbons is critical for a wide range of technologies, including supercapacitors and capacitive deionization for water desalination, yet many details remain poorly understood. For instance, an atomistic understanding of how ion selectivity is influenced by the molecular shape of ions, morphology of the micropores and applied voltages is largely lacking. In this work, we combined molecular dynamics simulations with enhanced sampling methods to elucidate the selectivity mechanism of nitrate and chloride in subnanometer graphene slit-pores. We show that nitrate is preferentially adsorbed over chloride in the slit-like micropores. This preferential adsorption was found to stem from the weaker hydration energy and unique anisotropy of the ion solvation of nitrate. Beside the effects of ion dehydration, we found that applied potential plays an important role in determining the ion selectivity, leading to a lower selectivity of nitrate over chloride at a high applied potential. We conclude that the measured ion selectivity results from a complex interplay between voltage, confinement, and specific ion effects-including ion shape and local hydration structure.

INTRODUCTION

Understanding ion transport and selectivity in porous materials is essential for a wide range of technologies, including energy storage and water purification.[1-8] As an example, among other water desalination technologies, capacitive deionization (CDI) offers a promising approach that utilizes charged porous electrodes to remove ionic species from aqueous solution through electrosorption.[9-11] This emerging technology has been considered as an efficient approach for treating brackish waters with a low or moderate salt concentration,[12, 13] and has demonstrated great potential for selective removal of target contaminants,[14-20] which is not readily achieved by other desalination technologies such as reverse osmosis.[21]

Over the last decade, major efforts in tailoring ion selectivity in porous materials have focused on size-based selectivity and functionalization of the pore entrance.[18, 20] A large number of studies suggests that ion selectivity in subnanometer pores is related to the differences in ion hydration and charge.[19, 22-28] In particular, variation in the selectivity of small ions has often been attributed to the effects of dehydration,[27-29] i.e., an ion with a smaller ionic radius acquires a greater charge density and stronger hydration shell, thereby undergoing lower dehydration at the pore entrance.[30] For example, investigations of Na^+, K^+ and NH_4^+ during the capacitive deionization process in micropores showed that electrorption capacity of the ions has an inveserve relation with their ionic radius.[31] In addition, significant effort has been devoted to investigate the role of ion valency on the selectivity. For instance, it has been shown that ions with a higher valency yields a higher electrosorption capacity due to stronger electrostatic interactions with the electrodes,[32] as suggested by the empirical Donnan model commonly used to model electrosorption of ions in microporous materials.[33]

More recent studies suggest that ion selectivity in porous materials can be more complex, as it may depend not only on ion charge and hydration but also on the shape of the ion and applied potential.[14, 34] For instance, by investigating the selectivity of NO_3^- and Cl^- in flow-through CDI (fteCDI) cells, Hawks *et al.*[14] and Mubita *et al.*[19] demonstrated that nitrate shows preferential sorption characteristics over chloride with nanoporous carbons.[14, 19] More importantly, these studies imply that pore size and morphology can have significant impact on adsorption selectivity, where the authors hypothesize that the trigonal planar molecular geometry of the nitrate molecule is responsible for its unique ability to fit in the narrow, slit-shaped pores present in the electrode materials. Finally, it was shown that the dependence of ion selectivity on the applied potential can be highly non-linear, as the selectivity of nitrate over chloride was found to decrease with higher applied voltages, an observation that cannot be simply explained based on the difference in the electrostatic interaction between the ions and electrode materials.[17] Overall, while these studies provide initital evidence of the dependence of ion selectivity on ion shape and applied potential, as well as a plausible explanation for the observations, it is clear that a detailed mechanistic understanding is lacking due to the complexity of the electrosorption process.

Besides experimental studies, a large number of molecular dynamics (MD) simulations have been devoted to the investigation of transport and structure of salt solutions in carbon-based slit pores. These studies have largely focused on simple, isotropic ions;[35-37] for instance, effects of charge density and slit pore size on the structures and partition have been reported for NaCl and $CaCl_2$ electrolytes.[38-41] However, to the best of our knowledge, the role of molecular shape of ions, which is associated with the anisotropy in the ion solvation, on transport mechanism and selectivity of ions in porous materials have not been investigated.[42]

In this work, we employed molecular dynamics simulations to provide a detailed understanding of the mechanism of NO_3^- and Cl^- selectivity in subnanometer slit-pores. Well-tempered metadynamics simulations of aqueous solutions at the interface with a 0.8 nm slit-pore show that NO_3^- yields a free energy barrier about two and a half times smaller than that of Cl^- to enter the pore. Our simulations provide direct evidence that this behavior stems from not only a weaker hydration energy of NO_3^-, but also a unique anisotropy of the ion solvation that leads to preferential sorption in the slit-like micropores. Besides the effects of ion dehydration, we demonstrate and discuss the importance of applied potential in determining the ion selectivity. On the basis of this information, we discuss possible strategies for improving the performance of carbon-based materials for ion selectivity.

METHODS

System setup

All-atom MD simulations were carried out using the LAMMPS package[43] patched with a version of PLUMED 2.5b[44] and OPLS-AA force fields.[45] The slit-pores were modeled as a stack of hydrophobic graphene layers that mimic hierarchical carbon aerogel monolith electrodes. The pore opening width is 0.8 nm, measured as center-of-mass distance between adjacent graphene layers, representing the subnanometer pores employed in the experimental study by Hawks *et al.*[14] The lateral dimensions of the graphene layers are approximately 3.1 nm x 3.3 nm. The graphene sheets were modeled as rigid structures without including any functional groups. In addition, two types of slit pores were used to study different aspects of ion adsorption and transport. The first one, which was used to understand the mechanism of ion transport and the calculation of transport barrier, has two open-ends and a charge-neutral structure. The other one was modeled to have only

one open-end and all of its carbon atoms were assigned to different charges to model ion adsorption at low and high applied potentials. Both sides of the slit pore were solvated by TIP3P water,[46] and Na^+, NO_3^- and Cl^- ions were randomly inserted to reach concentration of 1 M and neutralize the system. The system was first energy minimized and then equilibrated for 8 ns under NPT ensemble at T = 298.15 K and P = 1 atm. We note that the use of these water and ion model parameters yields ion solvation structure in good agreement with first-principles simulations. For instance, we obtained a value of 3.1 Å for the first maximum in the Cl^--oxygen radial distribution function (Figure S1), consistent with previous FPMD simulations.[47]

Free energy calculations

The free energy surface of ion transport through a slit pore was determined by using well-tempered metadynamics (WT-MetaD) simulations.[48] Here, metadynamics simulations were used to accelerate sampling of rare events by depositing a history-dependent bias energy in the form of Gaussian potential to the system's free energy landscape through predetermined collective variables (CVs):

$$V(s,t) = \sum_{k\tau<t} W(k\tau)\exp\left(-\sum_{i=1}^{d}\frac{\left(s_i - s_i(q(k\tau))\right)^2}{2\sigma_i^2}\right) \quad (1)$$

where σ is the width of the Gaussian for the i^{th} CV, τ is Gaussian addition rate, W is the height of the Gaussian and $s_i\big(q(k\tau)\big)$ corresponds to the value of CV obtained from the configuration of the system at time $k\tau$. In this way, the normal evolution of the system is biased in order to visit higher energy regions. In the conventional metadynamics approach,[49] the Gaussian of constant height is added during the entire simulation time, which may over bias the system. For instance, it is known that the use of a large Gaussian hill height may cause system destabilization or lead to false convergence.[50] In this work, we instead employed the WT-MetaD approach to ensure an

asymptotic convergence of the PMF.[51] Here, the height of the Gaussian is tempered with the simulation time as following:

$$W(k\tau) = W_0 \exp\left(-\frac{V(s(q(k\tau),k\tau)}{k_B \Delta T}\right), \quad (2)$$

where W_0 is the initial Gaussian height, ΔT is a temperature-dependent parameter affecting bias factor ($\gamma = \frac{T+\Delta T}{T}$) that tunes the rate of decreasing the Gaussian height, T is the system temperature and k_B is the Boltzmann constant.

The two-dimensional (2D) potential of mean force (PMF) for ion transport through a slit pore was evaluated by averaging the results from two independent ~500 ns WT-MetaD simulations. One-dimensional (1D) PMF was then obtained by calculating the minimum free energy path on the 2D PMF. In all simulations, two CVs were employed to facilitate PMF convergence[52] as we discuss in more detail below. The Gaussian bias energy is deposited every 500 steps with a height of 0.03585086 kcal/mol for Cl^- and Na^+, and 0.0239006 kcal/mol for NO_3^-. The height of the Gaussian potential is tempered with a bias factor of 10 for for Cl^- and Na^+, and 6 for NO_3^-.

RESULTS AND DISCUSSION

Selection of collective variables

Our WT-MetaD simulations were carried out using two CVs, which have been shown to provide more reliable results than the use of a single CV.[52] For the planar NO_3^- ion, we used CVs that describe the center-of-mass (COM) translation and molecular reorientation of the ion during transport through the pore (Figure 1A,B). For the latter, the CV was defined as the angle between the vector normal to the graphene surface and the one connecting the nitrogen atom and one of the oxygens of the nitrate ion (Figure 1B). For the spherical Cl^- ion, besides the CV that describes

COM translational motion, we used the number of water molecules in the first solvation shell as another CV (Figure 1C), given that dehydration has been often found to be a major barrier for ion permeation through narrow pores.[53] Here, the coordination number between water molecules and Cl^- ion was described as follows to prevent the discontinuity in the derivative of the calculated CV.

$$CV = \sum_{i \epsilon A} \sum_{i \epsilon B} s_{ij} \quad (3)$$

$$s_{ij} = \frac{1-\left(\frac{r_{ij}-d_0}{r_0}\right)^n}{1-\left(\frac{r_{ij}-d_0}{r_0}\right)^m} \quad (4)$$

where s_{ij} is 1 or 0 depending on existence of a contact between atoms i and j, r_{ij} is distance between atoms, r_0 is cut-off parameter, which is set to be 0.37 nm for the distance between the ion and oxygens of water molecules (see Figure S1). Other parameters (d_0, n and m) are related to the switching function and were set to be default values (0, 6 and 12, respectively). All three CVs are illustrated in Figure 1.

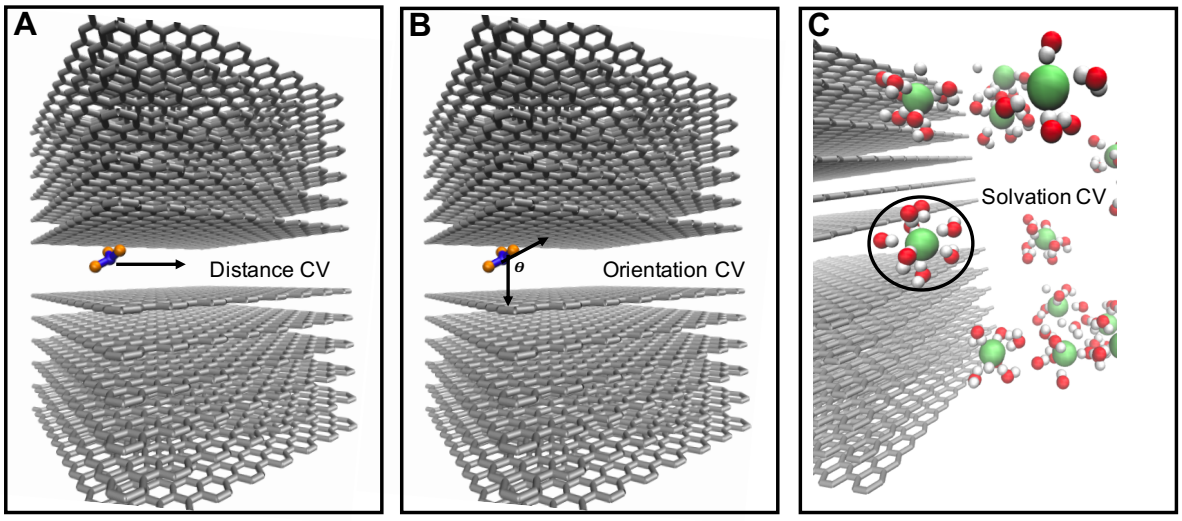

Figure 1. Definitions of the collective variables used in this work for the description of nitrate (A, B) and chloride (C) transport through a slit pore. The color key is red = oxygens bound to hydrogens, white = hydrogen, green = chloride, blue = nitrogen, orange = oxygens bound to nitrogen, and gray = carbon.

Potential of mean force (PMF) from all-atom simulations

The PMF was computed for the simulation systems shown in Figure 2A, consisting of an aqueous solution (NaCl or $NaNO_3$) and a slit pore with a width of 0.8 nm. Two randomly initialized WTMetaD replicas were run for 500 ns and the resulting two-dimensional PMF (2D PMF) (Figures 3 and 4) was obtained by averaging all the replicas for NO_3^- and Cl^-. The minimum free energy path (MFEP) of the 2D PMF (black curve in Figures 3 and 4) was calculated by using a zero-temperature string method, which represents the most probable transition path of the transport process. In addition, the 1D PMF was directly obtained by using the average MFEP from the WTMetaD replicas (Figure 5). We also note that ion transport through the slit-pore occurred multiple times and from both sides of the pore during the simulations, which ensures the convergence of the calculated PMFs. Our simulations also show that the standard deviation of the energy barrier obtained from multiple replicas are less than 0.5 k_BT.

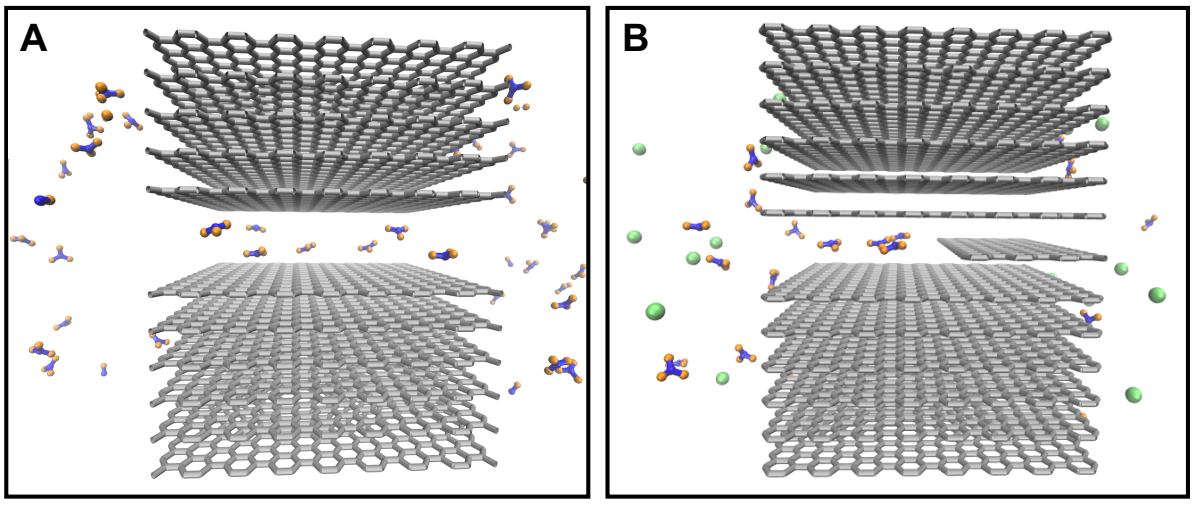

Figure 2. All-atom structures of slit pores made of graphene layers (gray) and aqueous solutions composed of water molecules, Na^+, NO_3^- (blue and orange) and Cl^- (green) ions. Water molecules and Na^+ ions are not shown for clarity. (A) Slit pore with two open-ends and either NaCl or $NaNO_3$ aqueous solutions, (B) slit pore with one open-end and a mixture of NaCl and $NaNO_3$ aqueous solutions. The systems shown in (A) and (B) were used for the calculation of energy barrier for ion transport and ion adsorption in the 0.8 nm slit-pore, respectively.

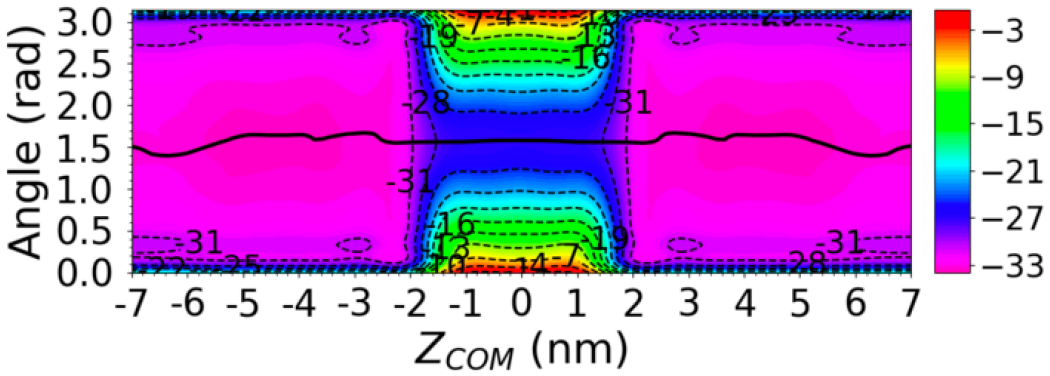

Figure 3. Two-dimensional free energy profiles of NO_3^- transport through a slit pore with a pore size of 0.8 nm. Y-axis (angle) describes the orientation of NO_3^- with respect to the slit pore and X-axis (Z_{COM}) describes center-of-mass distance between NO_3^- and the slit pore. The black line represents the minimum free energy path (MFEP). The energy is shown in the unit of kJ/mol. Different colors correspond to various energy levels, the lowest and highest energy values are shown by pink and red, respectively.

The calculated MFEP of NO_3^- (Figure 3) shows that NO_3^- favors the configuration with the molecular plane paralleled with the graphene surface during transport through the slit pore. In addition, the energy barrier for the transport of NO_3^- was found to be ~ 5.5 kJ/mol from the averaged MFEPs (Figure 5). We also estimated the energy barrier for transportation of NO_3^- in other molecular orientations. As expected, we found that the barrier for ion transport increases as the molecular plane of the ion becomes perpendicular to the pore surface (Figure 6). Overall, the lowest free energy on the 2D PMF corresponds to the configuration where the planar surface of NO_3^- is parallel to the graphene surface, indicating that the transport process is dominated by the orientation of NO_3^- in the slit pore.

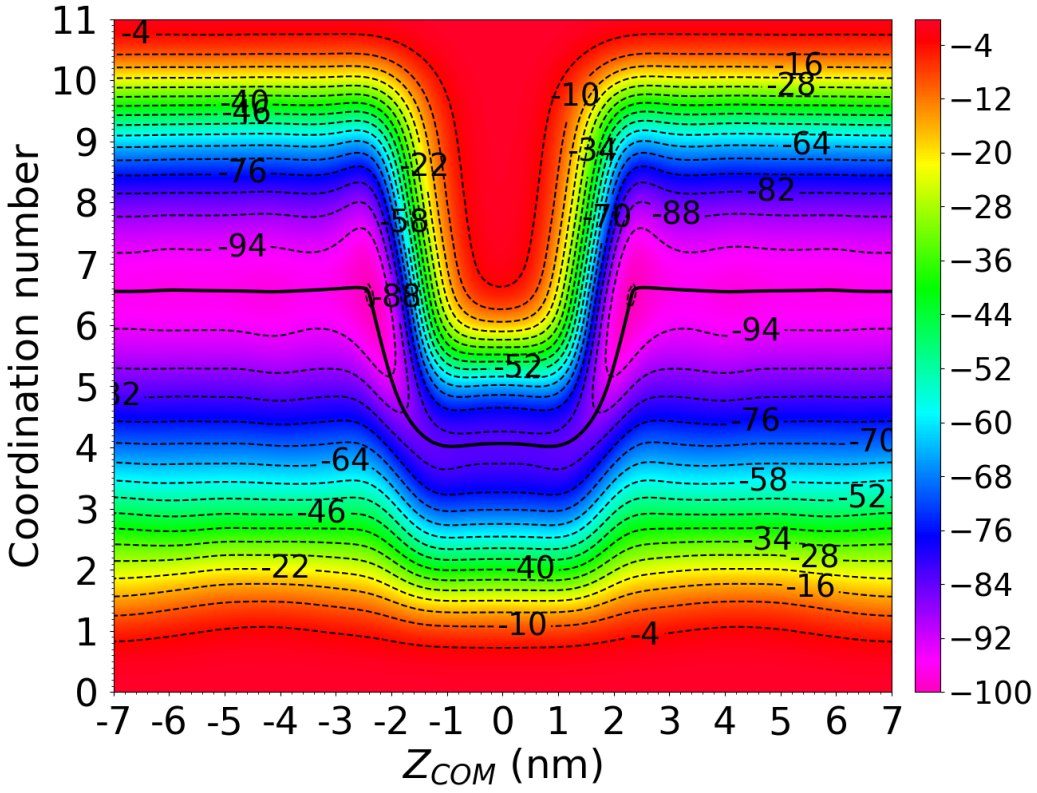

Figure 4. Two-dimensional free energy profiles of Cl^- transport through a slit pore with a size of 0.8 nm. Y-axis (coordination number) describes number of water molecules in the first solvation shell of Cl^- and X-axis (Z_{COM}) describes center-of-mass distance between Cl^- and the slit pore. The black line represents the minimum free energy path (MFEP). The energy is shown in the unit of kJ/mol. Different colors correspond to various energy levels, the lowest and highest energy values are shown by pink and red, respectively.

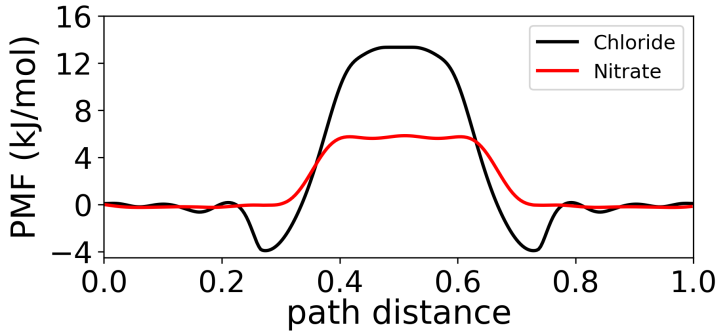

Figure 5. One-dimensional free energy profiles of NO_3^- and Cl^- transport through a slit pore with a size of 0.8 nm as a function of path distance obtained through the MFEPs from the 2D PMFs.

As Cl^- ion has no preferred orientation due to its shape, we used the coordination number between Cl^- and water molecules in the first solvation shell as the CV during transport. We found that Cl^- loses about 2-3 water molecules during transport through the slit pore (Figure 4), yielding an energy barrier of ~13.5 kJ/mol associated with the dehydration process. This energy barrier obtained for Cl^- is around 2.5 times larger than that of NO_3^-, indicating that both NO_3^- and Cl^- undergo a dehydration process while entering the slit pore, however, the free energy cost for this process is much higher for Cl^-. Although the hydration energy of NO_3^- is weaker than Cl^- (300 kJ/mol compared to 340 kJ/mol),[54] as we show below, it is not fully responsible for the large difference in the energy barrier between the two ions at the entrance. This is likely different from simple spherical ions, where the barrier for ion transport is largely governed by the difference in the hydration energy; for instance, we found that the barrier for Na^+ to transport into the pore is around 18 kJ/mol, which is slightly larger than that of Cl^- due to a stronger hydration energy (Figure S2).

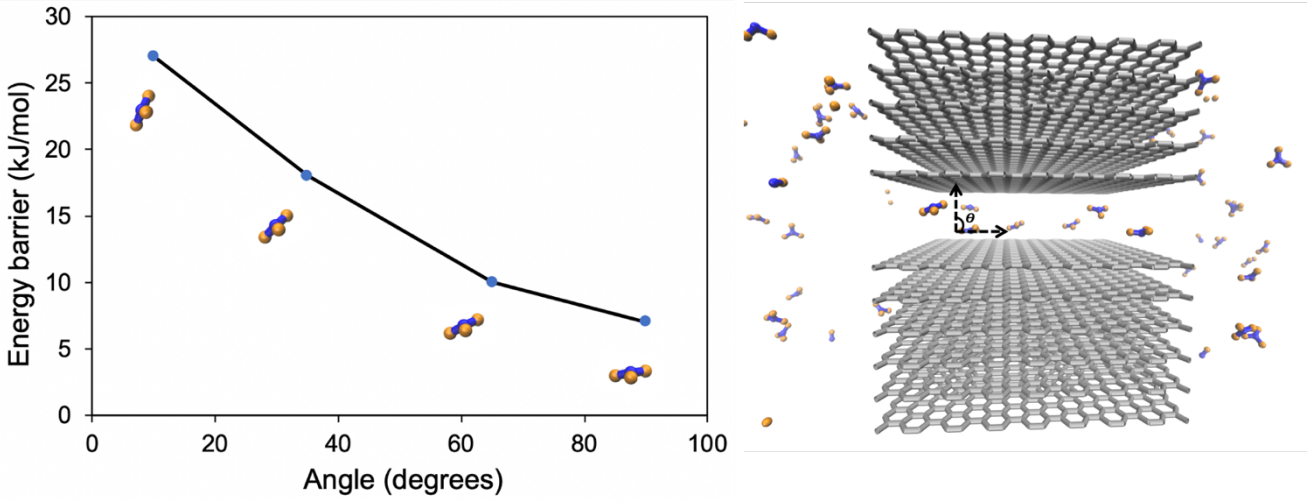

Figure 6. Energy barrier of NO_3^- transport through a slit pore as a function of the orientation of NO_3^-. The orientation is schematically described on the right. The values for the energy barrier were obtained by using the 2D free energy profile, shown in Figure 3. Water molecules were not shown for clarity.

The Role of Confinement in Solvation Properties of Ions

To understand the effect of confinement on ion solvation properties in more detail, and how dehydration influences the energy barrier for ion transport, we investigated water orientation and coordination number in the first solvation shell of the ions. Here, the number of water molecules surrounding NO_3^- and Cl^- were calculated by using a cut-off distance of 4.5 Å and 3.7 Å between oxygen atoms from water and the central nitrogen atom and Cl^-, respectively. These cut-off distances were chosen based on the first minimum of radial distribution functions between the ions and oxygen atoms of water molecules (Figure S1). For Cl^-, the coordination number can be explicitly extracted from the calculated 2D PMF, which is a function of the water coordination number and COM distance between the ion and slit pore (Figure 4). The PMF shows that, on average, Cl^- loses about 2.4 water molecules when entering the pore, as compared to a total ~6.6 water molecules in the first solvation shell in the bulk solution. Similarly, we found that NO_3^- ions lose about 2 water molecules on average when they enter the pore, as compared to a coordination number of ~7.8 water molecules in the bulk. This smaller dehydration degree at the entrance and a weaker hydration energy of NO_3^- is consistent with a lower energy barrier of the NO_3^- ion compared to Cl^-.

Notably, we found that most of water molecules that are removed from the first solvation shell of NO_3^- belong to the region above or below the planar surface of the ion, as shown in the Supporting Information (Movie S1). The orientation of water molecules around NO_3^- in the pore was further quantified by measuring the angle between a vector pointing from water oxygens to the nitrogen atom of NO_3^- and the vector perpendicular to the graphene surface (Figure 7). The angle distribution was found to shift towards 90 degrees as NO_3^- transports through the slit pore, indicating that water molecules are located in the plane of NO_3^-. We note that water molecules also prefer to occupy the molecular plane compared to the region above and below NO_3^- in the bulk

solution (see Figure S3).[14] This indicates that water molecules that are removed from the first solvation shell of NO_3^- are weakly bound to the ion, effectively leading to a lower energy barrier to enter the pore compared to that of Cl^-, despite the similar number of water molecules removed in both cases. Collectively, we conclude that a weaker hydration energy and a unique anisotropy of the solvation of NO_3^-, where water molecules prefer to reside on the molecular plane of the ion, is responsible for a preferential adsorption of NO_3^- over Cl^- in the slit-pores.

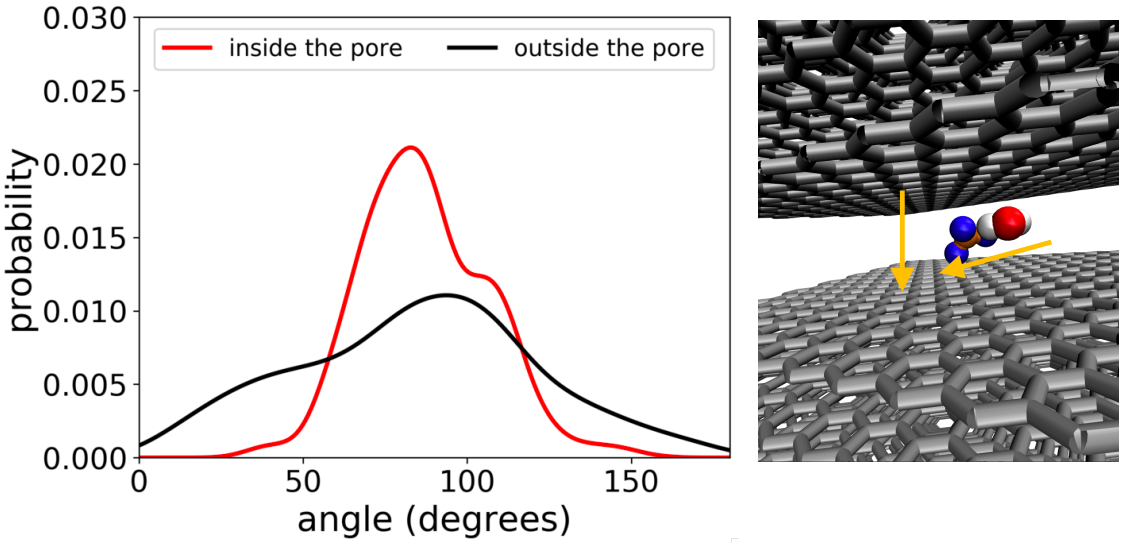

Figure 7. Probability distribution of orientations of water molecules surrounding NO_3^- when NO_3^- ions are located inside (red curve) or outside (black curve) the pore. The orientation is described by an angle defined by two vectors shown in the schematic on the right.

The Role of Applied Voltage in Selectivity of Ions

We now turn to discuss how ion selectivity is governed by the applied potential. Here, we investigated ion adsorption in the pore at two charge-densities, which represent low and high voltages in experiments, by using constant charge simulations.[55] The simulation systems for the selectivity work consist of an aqueous solution composed of NaCl and $NaNO_3$ mixture (1:1) and a 0.8 nm slit pore made of hydrophobic graphene layers with one open-end that represents the

carbon electrodes employed by Hawks *et al.*[14] (Figure 2B). Each carbon atom is assigned to 0.0025 -*e* and 0.006 -*e* to model low (~0.4 V) and high (~1.0 V) applied potentials, respectively.

Calculation of the number of adsorbed ions inside the pore (Figure 8) shows that there is only adsorption of NO_3^- for a low charge density (0.0025 -*e* per carbon atom) that represents the low applied potential (~0.4 V). However, adsorption of Cl^- is observed when the charge density is increased to 0.006 -*e* per carbon atom (~1.0 V), indicating that the electrodes have an increasing affinity for Cl^- ions as the charge density per carbon atom is increased (Figure 8). This is due to stronger ion-pore electrostatic interactions that overcome the energy penalty associated with the dehydration of Cl^-. Similarly, we found that the increase in the positive charge also lead to enhancement in the NO3- adsorption. On the other hand, we also found show that the use of negative charges does not lead to anion adsorption due to the strong electrostatic repulsion, but it results in the adsorption of Na+ as the counter ion (Figure S4). Our results are consistent with previous experimental findings,[14] showing that the use of a higher applied voltage in porous carbons leads to a decrease in the selectivity of the NO_3^- ion over Cl^-.[17] We note that Hawks *et al.*[14] experimentally observed a small amount of Cl^- adsorption at an applied potential of 0.6 V; we attribute this difference between our simulation results and experiment to the presence of wider pore sizes in experimental measurements (Figure S5). To confirm this hypothesis, we investigated adsorption of the ions in the wider pore of 1.1 nm. The simulations show a slight amount of chloride adsorption (Figure S6), indicating that these larger pores are responsible for chloride adsorption at a low applied potential. These results also suggest that a higher selectivity of nitrate over chloride at low applied potential can be achieved by using material with a smaller pore size distribution.

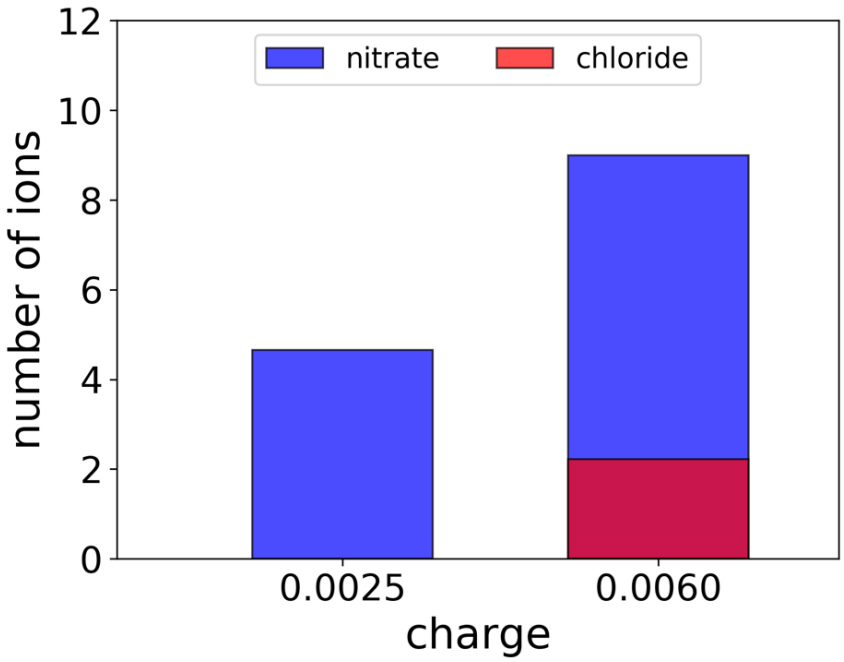

Figure 8. Number of NO_3^- and Cl^- ions inside the pore at two different charges, 0.0025 and 0.006 -*e*/carbon.

We conclude that the loss in NO_3^- selectivity over Cl^- at high applied voltages is due to a competition between ion-pore electrostatic interactions and specific ion effects, including ion hydration, size and shape. At zero or low applied potential, our simulations show that there is no Cl^- adsorption due to a high energy barrier for the ion to be dehydrated compared to that of NO_3^-. On the other hand, as the applied potential is increased, the ion-pore electrostatic interactions start to overcome the dehydration penalty, leading to Cl^- adsorption. Accordingly, although NO_3^- adsorption also increases with applied potential, its overall selectivity over Cl^- is reduced due to the presence of Cl^- in the pore. Interestingly, our results are consistent with a CDI theory proposed by Suss *et al.*,[26] where it is shown that ion selectivity is governed by a fine balance between ion volume exclusion and electrostatic effects. Overall, our simulations indicate that the inclusion of

ion size and shape, ion hydration, as well as pore size and shape in the CDI theory is highly important toward optimizing and predicting selectivity of ionic species in charged micropores.

CONCLUSIONS

In conclusion, we combined molecular dynamics simulations with enhanced sampling methods to elucidate the mechanism of nitrate and chloride selectivity in subnanometer graphene slit-pores. Our simulations provide direct evidence that nitrate is preferentially electrosorbed over chloride in the pores. Notably, the use of metadynamics simulations enables access to high resolution of the potential energy surface of the ions near the pores, providing insights into the correlation between ion selectivity, molecular shape, and morphology of the pores. Specifically, we showed that selectivity of nitrate over chloride stems from not only a weaker hydration energy of nitrate, but also a unique anisotropy of the ion solvation that leads to preferential adsorption in the slit-like micropores. Besides the effects of ion dehydration, we found that applied potential plays an important role in determining the ion selectivity, leading to a lower selectivity of nitrate over chloride at a high applied potential.

Our simulations also provide several key conclusions for ion transport and selectivity. We show that the energy barrier for ion transport into nanopores depends not only on the pore size and shape, but also on ion properties beyond the hydration energy. In particular, transport of ions with large hydration energy, such as Cl^-, is generally more energetically expensive than for larger, less strongly hydrated ions, such as NO_3^-. However, our calculations also point to the importance of the anisotropy of the ion solvation in ion selectivity; specifically, our study shows that the use of narrow slit pores can further facilitate NO_3^- adsorption due to the unique molecular shape and anisotropy in the solvation of the ion. These results have important implications in tuning

morphology of porous materials for selective removal of other complex ions from water, for instance. Finally, an interesting avenue for future studies is to investigate the role of other pore sizes as well as chemical functional groups at the entrance on the transport of more complex ions with different shapes and valency. Along these lines, it is also of interest to understand how energetics of ion transport is influenced by the choice of theoretical models employed for the description of ions and water.

CONFLICTS OF INTEREST

There are no conflicts of interest to declare.

ACKNOWLEDGEMENTS

This work was performed under the auspices of the U.S. Department of Energy by Lawrence Livermore National Laboratory under Contract DE-AC52-07NA27344. Financial support is from the Laboratory Directed Research and Development project (18-ERD-024). Computational support was from the LLNL Grand Challenge Program. The authors thank Liam Krauss for his critical reading of the manuscript.

REFERENCES

1. S. Faucher, N. Aluru, M. Z. Bazant, D. Blankschtein, A. H. Brozena, J. Cumings, J. P. de Souza, M. Elimelech, R. Epsztein, J. T. Fourkas, A. G. Rajan, H. J. Kulik, A. Levy, A. Majumdar, C. Martin, M. McEldrew, R. P. Misra, A. Noy, T. A. Pham, M. Reed, E. Schwegler, Z. Siwy, Y. H. Wang and M. Strano, *Journal of Physical Chemistry C*, 2019, **123**, 21309-21326.
2. G. Hummer, J. C. Rasaiah and J. P. Noworyta, *Nature*, 2001, **414**, 188-190.
3. B. Corry, *J Phys Chem B*, 2008, **112**, 1427-1434.
4. M. Elimelech and W. A. Phillip, *Science*, 2011, **333**, 712-717.

5. S. Porada, R. Zhao, A. van der Wal, V. Presser and P. M. Biesheuvel, *Progress in Materials Science*, 2013, **58**, 1388-1442.
6. P. Simon and Y. Gogotsi, *Nat Mater*, 2008, **7**, 845-854.
7. P. Simon and Y. Gogotsi, in *Nanosciense and Technology*, DOI: 10.1142/9789814287005_0033, pp. 320-329.
8. P. Simon and Y. Gogotsi, *Acc Chem Res*, 2013, **46**, 1094-1103.
9. M. E. Suss, S. Porada, X. Sun, P. M. Biesheuvel, J. Yoon and V. Presser, *Energy & Environmental Science*, 2015, **8**, 2296-2319.
10. M. A. Anderson, A. L. Cudero and J. Palma, *Electrochimica Acta*, 2010, **55**, 3845-3856.
11. P. Xu, J. E. Drewes, D. Heil and G. Wang, *Water Res*, 2008, **42**, 2605-2617.
12. Y. Oren, *Desalination*, 2008, **228**, 10-29.
13. S. Porada, L. Zhang and J. E. Dykstra, *Desalination*, 2020, **488**, 114383.
14. S. A. Hawks, M. R. Ceron, D. I. Oyarzun, T. A. Pham, C. Zhan, C. K. Loeb, D. Mew, A. Deinhart, B. C. Wood, J. G. Santiago, M. Stadermann and P. G. Campbell, *Environ Sci Technol*, 2019, **53**, 10863-10870.
15. D. I. Oyarzun, A. Hemmatifar, J. W. Palko, M. Stadermann and J. G. Santiago, *Water Res X*, 2018, **1**, 100008.
16. X. D. Zhang, K. C. Zuo, X. R. Zhang, C. Y. Zhang and P. Liang, *Environmental Science-Water Research & Technology*, 2020, **6**, 243-257.
17. M. R. Ceron, F. Aydin, S. A. Hawks, D. I. Oyarzun, C. Loeb, A. Deinhart, C. Zhan, T. A. Pham, M. Stadermann and P. G. Campbell, *ACS Appl Mater Interfaces*, 2020, DOI: 10.1021/acsami.0c07903.
18. J. W. Palko, D. I. Oyarzun, B. Ha, M. Stadermann and J. G. Santiago, *Chemical Engineering Journal*, 2018, **334**, 1289-1296.
19. T. M. Mubita, J. E. Dykstra, P. M. Biesheuvel, A. van der Wal and S. Porada, *Water Res*, 2019, **164**, 114885.
20. D. I. Oyarzun, A. Hemmatifar, J. W. Palko, M. Stadermann and J. G. Santiago, *Separation and Purification Technology*, 2018, **194**, 410-415.
21. A. Ramachandran, D. I. Oyarzun, S. A. Hawks, P. G. Campbell, M. Stadermann and J. G. Santiago, *Desalination*, 2019, **461**, 30-36.
22. Y. Shilina, M. D. Levi, V. Dargel, D. Aurbacha, S. Zavorine, D. Nucciarone, M. Humeniuk and I. C. Halalay, *Journal of the Electrochemical Society*, 2013, **160**, A629-A635.
23. G. Salitra, A. Soffer, L. Eliad, Y. Cohen and D. Aurbach, *Journal of the Electrochemical Society*, 2000, **147**, 2486-2493.
24. R. Lin, P. L. Taberna, J. Chmiola, D. Guay, Y. Gogotsi and P. Simon, *Journal of the Electrochemical Society*, 2009, **156**, A7-A12.
25. R. Zhao, M. van Soestbergen, H. H. Rijnaarts, A. van der Wal, M. Z. Bazant and P. M. Biesheuvel, *J Colloid Interface Sci*, 2012, **384**, 38-44.
26. M. E. Suss, *Journal of The Electrochemical Society*, 2017, **164**, E270-E275.
27. L. A. Richards, A. I. Schafer, B. S. Richards and B. Corry, *Small*, 2012, **8**, 1701-1709.
28. C. Song and B. Corry, *J Phys Chem B*, 2009, **113**, 7642-7649.
29. C. Zhan, M. R. Ceron, S. A. Hawks, M. Otani, B. C. Wood, T. A. Pham, M. Stadermann and P. G. Campbell, *Nat Commun*, 2019, **10**, 4858.
30. B. Tansel, J. Sager, T. Rector, J. Garland, R. F. Strayer, L. F. Levine, M. Roberts, M. Hummerick and J. Bauer, *Separation and Purification Technology*, 2006, **51**, 40-47.

31. Y. Z. Li, C. Zhang, Y. P. Jiang, T. J. Wang and H. F. Wang, *Desalination*, 2016, **399**, 171-177.
32. C. H. Hou and C. Y. Huang, *Desalination*, 2013, **314**, 124-129.
33. P. M. Biesheuvel, Y. Fu and M. Z. Bazant, *Phys Rev E Stat Nonlin Soft Matter Phys*, 2011, **83**, 061507.
34. R. Epsztein, E. Shaulsky, M. Qin and M. Elimelech, *Journal of Membrane Science*, 2019, **580**, 316-326.
35. S. Sahu, M. Di Ventra and M. Zwolak, *Nano Lett*, 2017, **17**, 4719-4724.
36. S. Sahu and M. Zwolak, *Nanoscale*, 2017, **9**, 11424-11428.
37. J. H. Park, S. B. Sinnott and N. R. Aluru, *Nanotechnology*, 2006, **17**, 895-900.
38. R. K. Kalluri, T. A. Ho, J. Biener, M. M. Biener and A. Striolo, *Journal of Physical Chemistry C*, 2013, **117**, 13609-13619.
39. R. K. Kalluri, D. Konatham and A. Striolo, *Journal of Physical Chemistry C*, 2011, **115**, 13786-13795.
40. Z. Bo, H. Yang, S. Zhang, J. Yang, J. Yan and K. Cen, *Sci Rep*, 2015, **5**, 14652.
41. G. A. Feng, R. Qiao, J. S. Huang, B. G. Sumpter and V. Meunier, *Journal of Physical Chemistry C*, 2010, **114**, 18012-18016.
42. F. Aydin, C. Zhan, C. Ritt, R. Epsztein, M. Elimelech, E. Schwegler and T. A. Pham, *Phys Chem Chem Phys*, 2020, **22**, 2540-2548.
43. S. Plimpton, *Journal of Computational Physics*, 1995, **117**, 1-19.
44. G. A. Tribello, M. Bonomi, D. Branduardi, C. Camilloni and G. Bussi, *Computer Physics Communications*, 2014, **185**, 604-613.
45. W. L. Jorgensen, D. S. Maxwell and J. TiradoRives, *Journal of the American Chemical Society*, 1996, **118**, 11225-11236.
46. W. L. Jorgensen, J. Chandrasekhar, J. D. Madura, R. W. Impey and M. L. Klein, *Journal of Chemical Physics*, 1983, **79**, 926-935.
47. T. A. Pham, T. Ogitsu, E. Y. Lau and E. Schwegler, *J Chem Phys*, 2016, **145**, 154501.
48. A. Barducci, G. Bussi and M. Parrinello, *Phys Rev Lett*, 2008, **100**, 020603.
49. A. Laio and M. Parrinello, *Proc Natl Acad Sci U S A*, 2002, **99**, 12562-12566.
50. R. Sun, J. F. Dama, J. S. Tan, J. P. Rose and G. A. Voth, *J Chem Theory Comput*, 2016, **12**, 5157-5169.
51. J. F. Dama, M. Parrinello and G. A. Voth, *Phys Rev Lett*, 2014, **112**, 240602.
52. F. Aydin, R. Sun and J. M. J. Swanson, *Biophys J*, 2019, **117**, 87-98.
53. Z. Li, Y. Li, Y. C. Yao, F. Aydin, C. Zhan, Y. Chen, M. Elimelech, T. A. Pham and A. Noy, *ACS Nano*, 2020, **14**, 6269-6275.
54. Y. Marcus, *J. Chem. Soc., Faraday Trans.*, 1991, **87**, 2995-2999.
55. C. Zhan, C. Lian, Y. Zhang, M. W. Thompson, Y. Xie, J. Wu, P. R. C. Kent, P. T. Cummings, D. E. Jiang and D. J. Wesolowski, *Adv Sci (Weinh)*, 2017, **4**, 1700059.